

Simulating Linear Sweep Voltammetry from First-Principles: Application to Electrochemical Oxidation of Water on Pt(111) and Pt₃Ni(111)

Venkatasubramanian Viswanathan,[†] Heine Anton Hansen,[‡] Jan Rossmeisl,[§] Thomas Francisco Jaramillo,[‡] Heinz Pitsch,[†] and Jens K. Nørskov*,^{‡,||}

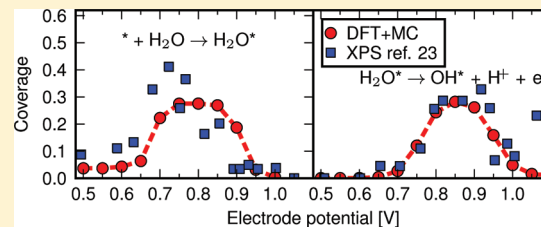
[†]Department of Mechanical Engineering, and [‡]Department of Chemical Engineering, Stanford University, Stanford, California 94305-3030, United States

[§]Center for Atomic-scale Materials Design, Department of Physics, Technical University of Denmark, DK-2800, Lyngby, Denmark

^{||}SUNCAT, SLAC National Accelerator Laboratory, Menlo Park, California 94025-7015, United States

Supporting Information

ABSTRACT: Cyclic voltammetry is a fundamental experimental method for characterizing adsorbates on electrochemical surfaces. We present a model for the electrochemical solid–liquid interface, and we simulate the linear sweep voltammogram of the electrochemical oxidation of H₂O on Pt(111) and Pt₃Ni(111), based on kinetic and thermodynamic parameters computed by Density Functional Theory (DFT) and the dynamics of the system solved through Monte Carlo-based methods. The model predicts onset of OH and O formation in good agreement with voltammetric and ex situ XPS experiments.



■ INTRODUCTION

Cyclic voltammetry is the most fundamentally important analytical method used to study electrode materials.^{1,2} There has been tremendous progress made in understanding the nature of the processes that cause peaks in a voltammogram.^{3,4} The voltammetric features can be used to assign the reversibility of a reaction, and to identify multistep charge transfer reactions and multicomponent systems.^{3,4} As ubiquitous as this method is in analytical electrochemistry, however, the exact faradaic process that causes the voltammetric peak is often difficult to conclusively assign. In a cyclic voltammogram (CV), current is measured as a function of applied potential, which is swept continuously; although the current can be measured with great accuracy, the molecular-scale surface processes that give rise to the current are difficult to identify conclusively. One of the reasons for this difficulty is that electrochemistry is conducted in a liquid cell that operates close to ambient temperature and pressure, preventing the use of a number of common spectroscopic and microscopic techniques that require high vacuum for operation. Another reason is that many of the surface processes involve adsorbates that are similar to, if not identical to, the surrounding liquid medium, making them difficult to follow unambiguously. Despite the development of advanced experimental methods, fundamental limits will always exist in detecting surface processes under true operating conditions.

Our approach presents a theoretical approach to derive cyclic voltammograms in an aqueous environment from first-principles. By accounting for the molecular-scale physics of interfacial processes in electrochemistry, this model provides

insight into the surface structure of adsorbed and interfacial water, OH, and O as a function of applied potential. The approach uses kinetic and thermodynamic parameters computed by Density Functional Theory (DFT), and the dynamics of the system is solved through a Monte Carlo-based method. This approach is used to simulate the oxidation of water on Pt(111) and Pt skin on Pt₃Ni(111) surfaces in the potential range 0.5–1 V. The fundamental surface processes involved relate directly to the catalytic activity of these surfaces toward electrocatalytic oxygen reduction⁵ and other aqueous electrochemical reactions.

■ MODEL APPROACH

The simulation of the kinetics of the oxidation of water is accomplished through a combination of equilibrium and Dynamic Monte Carlo (DMC) methods using kinetic and thermodynamic parameters calculated from Density Functional Theory (DFT). The combination of Monte Carlo methods is used to carry out an efficient time scale separation where the fast processes are handled in equilibrium and the slow kinetic steps are handled in the Dynamic Monte Carlo method. As a result of this separation, chemical and electrochemical surface processes in addition to adsorbate–adsorbate interactions can be handled efficiently.

Lattice-Gas Model of the Metal–Liquid Interface. The metal–liquid interface is modeled using a lattice gas

Received: November 9, 2011

Revised: January 13, 2012

Published: January 14, 2012

Hamiltonian approach, where the different kinds of water and OH present are shown in Figure 1. The water bilayer typically

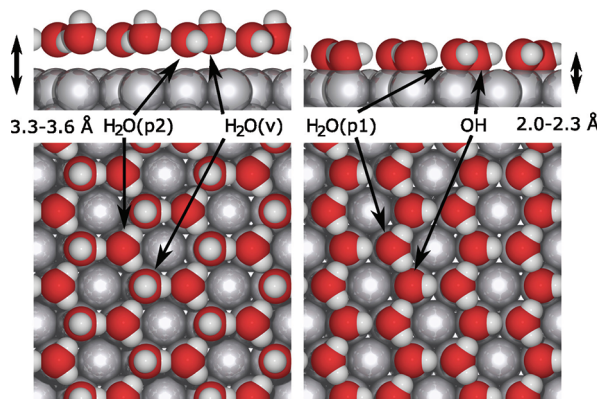


Figure 1. Hydrogen ordered ($\sqrt{3} \times \sqrt{3}$)R30° phases of H₂O–H₂O (left) and OH–H₂O (right) on Pt(111). The different types of water and OH have been labeled.

consists of two kinds of water: a water that is parallel to the surface and a water with a hydrogen atom pointing away or toward the electrode surface. The focus of our study is at positive electrode potentials, where we expect the electric field to favor the water with its hydrogen pointing away from the electrode surface.⁶ The two kinds of water in this structure are denoted by H₂O(p2) and H₂O(v). The formation of OH occurs in a phase transformation from ($\sqrt{3} \times \sqrt{3}$)R30° H₂O–H₂O phase to ($\sqrt{3} \times \sqrt{3}$)R30° OH–H₂O phase. This gives reversible potentials for OH adsorption that are in good agreement with experiments.⁶ This phase transformation happens through the oxidation of H₂O(v) to OH and a subsequent movement of H₂O(p2) to H₂O(p1). The main

difference between the two water molecules H₂O(p1) and H₂O(p2) is that H₂O(p1) has a bond distance to the Pt surface that is comparable to the H₂O monomer on Pt(111), whereas H₂O(p2) is further away from the surface, and is weakly adsorbed. We note that the distances reported here for the hydrogen ordered ($\sqrt{3} \times \sqrt{3}$)R30° phases of H₂O–H₂O and OH–H₂O are similar to those observed in MD simulations described previously.^{7–9} In addition, we also consider O to be adsorbed in fcc hollow sites.

Interactions of adsorbates with the surface are included through a lattice Hamiltonian given below:

$$H = \sum_i (E_{\text{ads}}^X + E_{\text{ato}}^X)c_i^X + \frac{1}{2} \sum_{\langle i,j \rangle} V_{ij}^{XY}(\theta_1, \theta_2)c_i^X(\theta_1) c_j^Y(\theta_2) + \frac{1}{2} \sum_{(i,j)} V^{\text{OX}}c_i^{\text{O}}c_j^{\text{X}} \quad (1)$$

where E_{ads}^X and E_{ato}^X are the adsorption energy and the atomization energy of the species X respectively, and c_i^X is the occupation number of X at site i. This is 1 if an adsorbate X is at site i and 0 otherwise. $V_{ij}^{XY}(\theta_1, \theta_2)$ is the interaction energy between adsorbates X and Y at sites i and j with adsorbate angles θ_1 and θ_2 as defined in Figure 2. The sum $\langle i,j \rangle$ runs over all pairs of nearest neighbor top sites. Interactions with O adsorbates are included in the last sum, where (i,j) includes up to next nearest neighbor sites. This approach is inspired by the work of Karlberg et al.^{10,11} who studied the water uptake and the kinetics of H₂O desorption from an O precovered Pt(111) surface using such an approach.

Karlberg et al. showed that second nearest neighbor interactions between OH–H₂O and OH–OH are less than 2% of the nearest neighbor interactions on Pt(111),¹² and we have neglected these interactions.

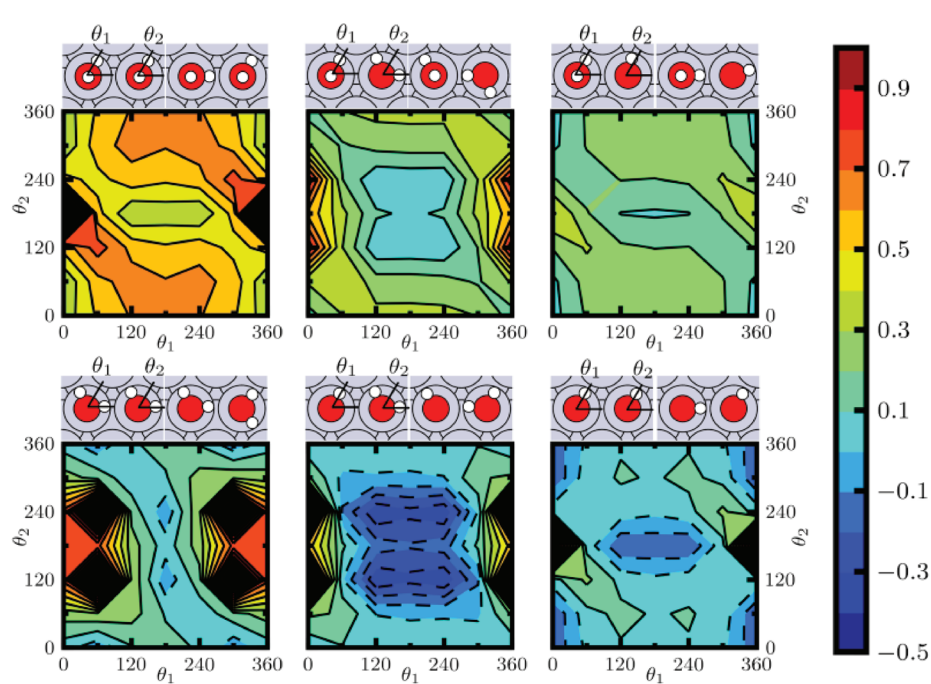
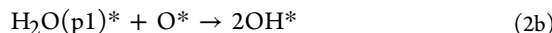


Figure 2. Angle-resolved interaction potentials (in eV) for H₂O(v)–H₂O(v), H₂O(v)–H₂O(p1), H₂O(v)–OH, H₂O(p1)–H₂O(p1), OH–H₂O(p1), and OH–OH on Pt(111). Angle-resolved interaction potentials between H₂O(p2) and other adsorbates are shown in the Supporting Information.

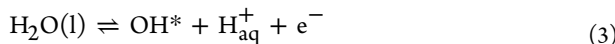
Surface Processes. Water diffusion is, in general, fast even at very low temperatures ($T \approx 25$ K).¹³ Water is believed to diffuse easily along the close packed directions.¹⁴ Michaelides et al. calculated the barrier for OH diffusion along the close packed rows of Pt(111) to be 0.1 eV, and that H diffusion in the OH–H₂O phase is very fast ($E_a < 0.01$ eV).¹⁴ They also found that the barrier for the rotation of a water monomer on Ru(0001) is 0.02 eV,¹⁵ and we expect a similar barrier on Pt(111). Thus, we treat the following fast processes in equilibrium:

- hydrogen transfer between adsorbed species:

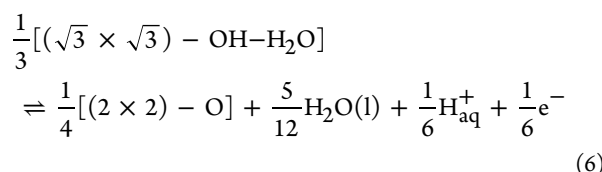
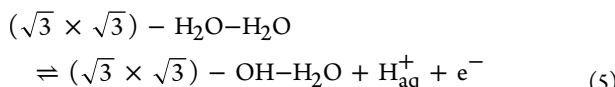


- diffusion and rotation of H₂O(p1), H₂O(p2), OH, and H₂O(v)
- diffusion between adjacent hollow sites
- interconversion of H₂O(p2), H₂O(p1), and H₂O(v)

The electrochemical reactions of the water discharge reaction shown in eqs 3 and 4 are treated kinetically.



Reversible Potentials. The rates for reactions 3 and 4 are calculated using local reaction center (LRC) theory¹⁶ as implemented in the CICV method¹⁷ and are taken from Rai et al.¹⁸ The activation energy varies linearly with potential in the potential range of interest. As we are interested in the surface coverages at dynamical equilibrium, we do not expect the results to depend appreciably on the specific method used for calculating the potential dependence of the rates. The ratios of the rates calculated from the CICV method are shifted to give the same reversible potentials as the thermodynamic method, described in the Supporting Information, for the following phase transitions between ordered phases:



The correction is similar to that used by Rai et al.,¹⁸ and is done because LRC theory does not properly include the stabilization of the final state and initial state due to hydrogen bonding in a water environment. It therefore gives reversible potentials that are much higher than the ones obtained from DFT calculations of the thermodynamics.

The formation of the ordered phases of $(\sqrt{3} \times \sqrt{3})R30^\circ$ OH–H₂O and (2×2) O are determined by the reversible potentials. The adsorbate interactions account for defect formation in these ordered adsorbate phases. Further, the interaction potentials allow the formation of structures other than the mentioned ordered phases.

Monte Carlo Simulations. Using the kinetic rates and adsorbate interactions calculated, we find the dynamical equilibrium at the surface set up by eqs 3 and 4 at each

potential of interest. Between each kinetic step, the surface is equilibrated by Metropolis Monte Carlo (MMC) simulations. The MMC simulations use an annealing procedure starting from 50 000 K and decrease the temperature in steps of 500 K until the final temperature of 300 K is reached. The simulations are done on a 50×50 hexagonal lattice with nonperiodic boundary conditions. It has been checked that the results are converged with respect to the lattice size. The simulations started from an equilibrated H₂O–H₂O structure with a total coverage of 0.6 ML. The potential is then increased in steps of 0.05 V, where the adsorbate coverages are converged at each potential in a cycle of DMC steps and MMC runs.

■ CALCULATION DETAILS

DFT Calculations. The angular-dependent nearest neighbor interactions between adsorbates are calculated following an approach outlined by Karlberg et al.^{10,11} The details of the approach and the calculation of the interaction parameters are described in the Supporting Information. The reversible potentials for the phase transformations are calculated using the RPBE functional for exchange and correlation¹⁹ and follow the method applied previously.^{6,20} The details of the method are discussed in the Supporting Information.

Dynamic Monte Carlo Method. The Dynamic Monte Carlo method pioneered by Gillespie²¹ enables the efficient solution of the time-evolution and the dynamics of chemical systems in a stochastic sense. Several algorithms have been subsequently developed for simulating catalyst systems, and all DMC simulations in this work use an efficient variant of the Variable Step Size Method (VSSM), called VSSMb.^{22,23} A more detailed discussion of the method can be found elsewhere.^{22–25} The details of the algorithm are presented in the Supporting Information.

■ RESULTS AND DISCUSSION

We begin by examining the interaction of different oxygen adsorbates and then discuss the structure of the adsorbate layer at different potentials. We subsequently discuss the simulated voltammetric features on Pt(111) and Pt₃Ni(111).

Interaction Potentials. A key feature determining the structure of the adsorbate layer is the highly attractive H₂O(p1)–OH interaction when H₂O(p1) is the hydrogen-bond donor. From the calculated interaction potentials shown in Figure 2, the formation of an extended H₂O(v)–H₂O(p1) $(\sqrt{3} \times \sqrt{3})R30^\circ$ phase from an extended H₂O(v)–H₂O(p2) $(\sqrt{3} \times \sqrt{3})R30^\circ$ phase costs 49 meV/H₂O(p), so there will be a mixed phase of H₂O(v)–H₂O(p1) and H₂O(v)–H₂O(p2) at room temperature. In a $(\sqrt{3} \times \sqrt{3})R30^\circ$ OH–H₂O environment, H₂O(p1) is more stable than H₂O(p2) by 1.02 eV. This shows that the formation of OH will be accompanied by the movement of H₂O(p2) to H₂O(p1). Further, the OH–H₂O(p1) interactions are more attractive than the OH–OH interactions. Thus, domains of OH–H₂O(p1) with a $(\sqrt{3} \times \sqrt{3})R30^\circ$ structure of the oxygen atoms will be formed.

To address the issue of the edges of the OH–H₂O(p1) islands, we find that H₂O(p1) with one OH neighbor and two H₂O(v) neighbors is stable relative to H₂O(p2) in the same environment by 0.46 eV. However, when OH is the hydrogen-bond acceptor, this stability is only 4 meV. Therefore, the edges of the OH–H₂O(p1) islands will be decorated by H₂O(p1). The calculated adsorbate–adsorbate interaction potentials also

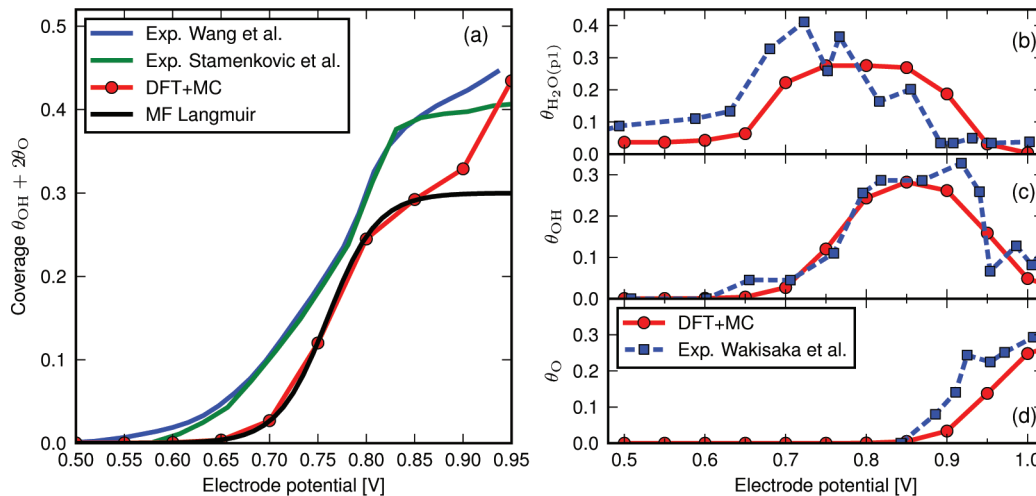


Figure 3. (a) Simulated integrated cyclic voltammogram for Pt(111). The electrode potential is measured vs RHE. The experiment shown from Wang et al.²⁶ and Stamenkovic et al.²⁷ (b)–(d) $\theta_{\text{H}_2\text{O}(\text{p}1)}$, θ_{OH} , and θ_{O} calculated from DFT+MC simulations as compared to ex situ EC-XPS experiments by Wakisaka et al.²⁸

show good overall agreement with similar potentials calculated by Karlberg et al.¹¹

Simulated Voltammogram on Pt(111). The simulated potential-dependent coverage of O-containing adsorbates on Pt(111) is shown in Figure 3a and is compared to the charge transfer from OH adsorption in the butterfly region between 0.6 V_{RHE} and 0.95 V_{RHE} in the linear sweep voltammetry experiments by Wang et al.²⁶ and Stamenkovic et al.²⁷ The coverages of OH, H₂O(p1), and O, shown in Figure 3b–d, agree well with the ex situ electrochemical XPS experiments of Wakisaka et al.²⁸

According to the model, as seen in Figure 3c, OH adsorbs between 0.65 V_{RHE} and 0.85 V_{RHE}. It is also seen that OH adsorption is accompanied by H₂O(p1) with the H₂O(p1) decorating the edges of the OH–H₂O(p1) islands. As a result, H₂O(p1) has a higher coverage, shown in Figure 3b, as compared to OH until the formation of the extended ($\sqrt{3} \times \sqrt{3}$)R30° OH–H₂O(p1). At higher potentials, further oxidation of OH to O leads to an effective repulsive interaction between adsorbed O and H₂O(p1). This results in a conversion of H₂O(p1) to its weakly adsorbed H₂O(p2) state, which is more stable in the O environment. This is in good agreement with the experiments by Wakisaka et al.²⁸ who observe a drop in the coverage of H₂O(p1) beyond 0.85 V_{RHE}. Wakisaka et al.²⁸ also find that oxygen formation starts between 0.85 V_{RHE} and 0.9 V_{RHE} in 0.1 M HF (hydrofluoric acid), which is in reasonable agreement with our simulations²⁸ as shown in Figure 3d.

The simulated coverage curve follows the integrated voltammogram quite well as seen in Figure 3a. However, the charge transfer at 0.6–0.75 V_{RHE} and at 0.8–0.9 V_{RHE} is lower than that obtained from the integration of the voltammogram. The characteristic sharp peak in the butterfly region of the voltammogram around 0.8 V_{RHE} corresponds in our model to the formation of 1/3 ML OH phase. The current spike has been suggested to be caused by an order–disorder transition²⁹ or by the interaction of the adsorbed OH with perchlorate.³⁰ However, recent DFT calculations have shown that perchlorate adsorption is thermodynamically unfavorable,³¹ and as the peak is also present in other electrolytes such as HF, the sharp peak at 0.8 V_{RHE} is most likely due to an order–disorder transition.

We speculate that at low potentials, the OH–H₂O(p1) islands are formed out of registry with each other. As the edges of these islands are decorated by H₂O(p1), at higher potentials, when these islands have to merge to form the extended OH–H₂O(p1) phase, the oxidation of the water present along the perimeter of these separated islands over a small potential range could lead to the current spike observed. However, our model cannot capture this as a long-range order is imposed by the water bilayer causing the different OH–H₂O(p1) domains to be formed in registry.

At 0.8 V_{RHE}, the charge from the integrated voltammogram is about 0.05 electrons per Pt atom larger than in our simulations. However, it should be noted that voltammogram does not measure the charge transfer from adsorption directly, but also contains contributions from variations in double layer capacitance with potential. Both electrochemical impedance spectroscopy and Frumkins thermodynamic method show that the double layer capacitance changes in the region of OH adsorption.^{31–33} OH coverages higher than those found in our model could also be caused by the formation of phase–antiphase domains with a higher local OH coverage at the domain boundaries or by coexistence of ($\sqrt{3} \times \sqrt{3}$)R30° domains and (1 × 1) OH domains. Periodic structures with higher OH coverage than 1/3 ML OH could in principle also be formed, for example, a (2 × 1) OH–H₂O structure with 0.5 ML OH, but the calculated interaction potentials do not favor this. In addition, more complicated structures involving multiple layers of H₂O, OH, and the counter-anions, could, in principle, be formed leading to additional charge transfer, which has not been considered in this study.

Our model predicts the increased oxidation of OH to O at 0.9 V_{RHE} as shown in Figure 4. This agrees well with the ex situ EC-XPS and in situ STM experiments in 0.1 M HF by Wakisaka et al.^{28,34} However, the peak in the voltammogram typically assigned to O is around 1.05 V_{RHE}.²⁷ It is also possible that the earlier detection of O in the experiments of Wakisaka et al. could be due to the presence of defects in the Pt(111) surface. It has been shown in the work of Björling et al.³⁵ that the presence of steps gives rise to current formation after the OH peak, which has been attributed by the authors to O formation on these steps. We also note that within our model,

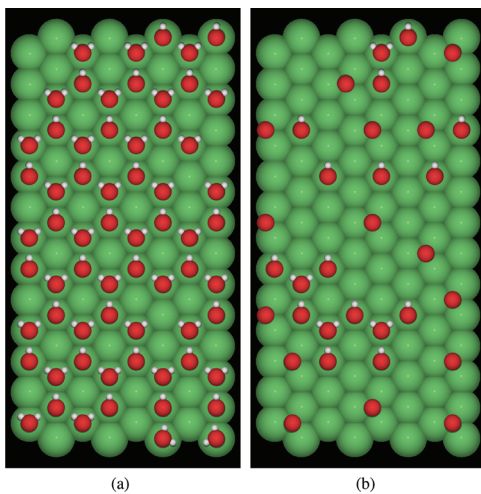


Figure 4. Snapshot of the adsorbate layer on Pt(111) formed from the simulated voltammogram at (a) 0.85 V_{RHE} and (b) 0.90 V_{RHE}. The Pt atoms are green, O are red, and H are white. H₂O(p2) and H₂O(v) are not shown.

the thermodynamic driving force is only 1/6 e⁻ per Pt site for the oxidation of (1/3 ML) OH to (1/4 ML) O as shown in eq 6, which is quite small, and the calculated reversible potential is therefore sensitive to DFT errors. It is difficult to conclusively assign the exact potential for the formation of O.

We note that a simple Langmuir isotherm can be used successfully for predicting the OH adsorption such as the one developed by Rossmeisl et al.³⁶ as shown in Figure 3. However, it can become rather complex to include the coadsorption of O and OH within the framework of such a simple model.

VOLTAMMOGRAM ON Pt₃Ni

The application of the developed approach to simulate the voltammogram on Pt skin on Pt₃Ni needs to additionally include the effect of solute concentration in the subsurface layers as theoretical calculations have indicated that these affect the binding energy of oxygen intermediates.³⁷ To fully comprehend the ligand effects of subsurface solute concentration on the voltammetry, a dynamical model capable of incorporating site heterogeneity is required.

Site Heterogeneity. To examine the effect of site heterogeneity, we have calculated the formation energy of OH at atop sites and O at fcc hollow sites on Pt₃Ni alloys. These are terminated with a 1 ML Pt skin with 0%, 25%, or

50% Ni in the second layer and bulk composition in the third and fourth layers. The Pt₃Ni alloy surface is shown in Figure 5, for a surface with 50% and 25% Ni in the second layer. The formation energies on the different adsorption sites are shown in Table 1. As a result, we model the surface in the Monte

Table 1. Formation Energies of O and OH in eV and Reversible Potentials in V_{RHE} on Pt₃Ni with a Pt Skin and Different Ni Concentrations in the Second Layer and on Compressed Pt and Uncompressed Pt^a

bulk: second layer Ni concn:	Pt ₃ Ni 50%	Pt ₃ Ni 25%	Pt ₃ Ni 0%	Pt 2.3%	Pt 0%
ΔE _{OH} ^A	1.18	1.22	1.15	1.16	1.08
ΔE _{OH} ^B	1.13	1.10	1.12	1.16	1.08
ΔE _{OH} ^C	1.30	1.22	1.15	1.16	1.08
ΔE _{OH} ^D	1.30	1.22	1.15	1.16	1.08
ΔE _O ^E	1.91	1.87	1.84	1.83	1.60
ΔE _O ^F	1.91	1.87	1.84	1.83	1.60
ΔE _O ^G	2.17	2.14	1.78	1.83	1.60
ΔE _O ^H	2.19	1.87	1.84	1.83	1.60
average ΔE _{OH}	1.22	1.19	1.14	1.16	1.08
average ΔE _O	2.04	1.94	1.83	1.83	1.60
U _{OH} ^{rev}	0.91	0.88	0.84		0.76
U _O ^{rev}	1.11	1.12	1.09		0.95

^aThe adsorption sites on Pt₃Ni are shown in Figure 5.

Carlo simulations by a (50 × 50) hexagonal lattice with heterogeneous sites with (2 × 2) periodicity.

In general, O and OH bind weaker on Pt₃Ni than on pure Pt and bind even weaker as the Ni content in the second layer increases. For Pt₃Ni depleted of Ni in the second layer, there is still a weakening of the binding energies relative to Pt and a dependence on the alloy structure below the second layer. The formation energy of O and OH is also shown for a 2.3% compressed Pt slab in Table 1. This corresponds to Pt with the lattice constant used in the DFT calculations for the Pt₃Ni alloy. It is seen that part of the destabilization of adsorbates relative to Pt comes from the compression of the Pt overlayer on Pt₃Ni. To estimate the effect of the lattice compression when going from Pt(111) to a Pt skin on Pt₃Ni on the interaction parameters, we calculate the H₂O(p1)–OH interaction potential and the H₂O(p1)–H₂O(p1) interaction potential on a 4 layer Pt slab compressed by 2.3%. Compression weakens the most attractive OH–H₂O(p1) interactions at ($\theta_1 \in \{120^\circ, 180^\circ, 240^\circ\}$, $\theta_2 = 120^\circ$) by 9

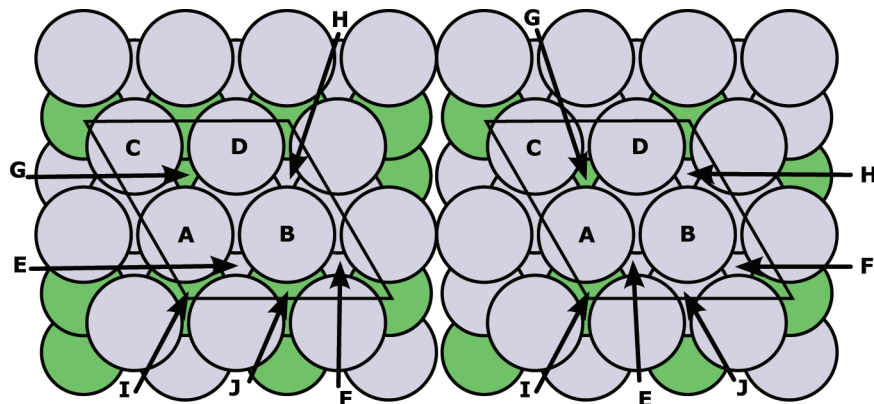


Figure 5. Heterogeneous adsorption sites at a Pt skin on Pt₃Ni with 50% Ni (left) and on Pt₃Ni with 25% Ni (right) in the second layer.

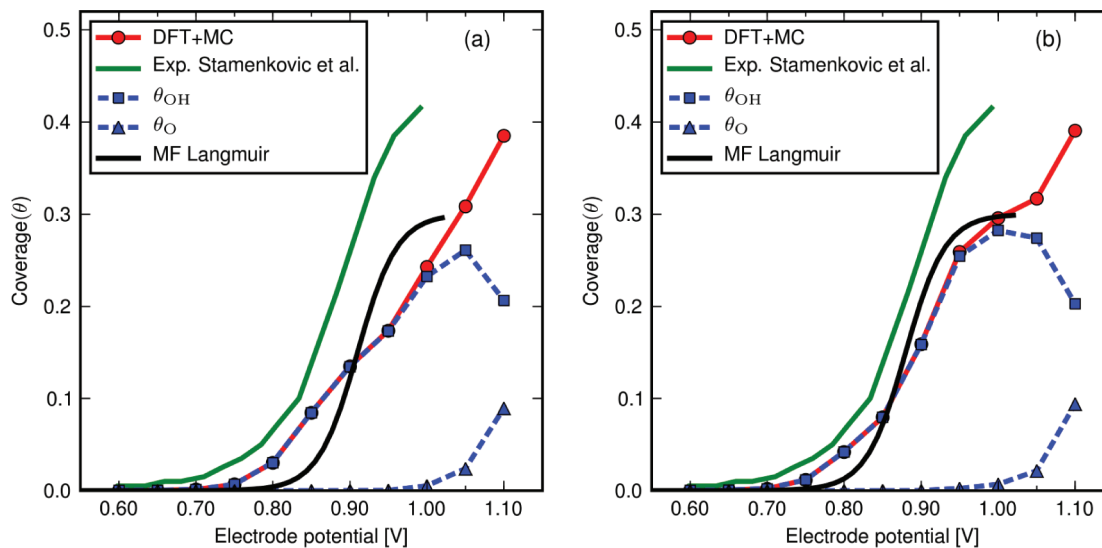


Figure 6. Simulated integrated cyclic voltammogram for Pt_3Ni with (a) 50% Ni and (b) 25% Ni in the second layer. The electrode potential is measured vs RHE. The experiment shown in the figure is by Stamenkovic et al.²⁷

meV. On the other hand, the most attractive $\text{H}_2\text{O}(\text{p}1)-\text{H}_2\text{O}(\text{p}1)$ interaction at ($\theta_1 = 60^\circ$, $\theta_2 = 0^\circ$) is strengthened by 15 meV. Because the interaction potentials are not strongly affected by lattice compression, the Monte Carlo simulations are done using the same interaction potentials V as those on Pt. Variations in the adsorption energy of $\text{H}_2\text{O}(\text{p}1)$ on Pt_3Ni with 50% Ni in the second layer were below 9 meV and have been neglected here.

From calculations of OH in the $(2\sqrt{3} \times 2\sqrt{3})\text{R}30^\circ$ OH– H_2O structure, we find a 0.15 V shift in the reversible potential for OH formation relative to Pt. This agrees well with the 0.13 V shift used by Rossmeisl et al.³⁶ For the extended OH– H_2O structure, OH is adsorbed on all possible top sites. Accordingly, we find a 0.14 eV shift in the average OH formation energy on Pt_3Ni relative to Pt, shown in Table 1. This shows that the shift in the reversible potential for the formation of OH in $(2\sqrt{3} \times 2\sqrt{3})\text{R}30^\circ$ OH– H_2O structure is described well by the shift in the average formation energy of OH. Therefore, for Pt_3Ni with 25% or 0% Ni in the second layer, we approximate the reversible potential for OH formation from the shift in average OH formation energy.

Figure 6 shows the simulated OH and O adsorption on Pt_3Ni with 50% Ni in the second layer and 25% Ni in the second layer. With 50% Ni in the second layer, the onset of OH adsorption is offset by \sim 50 mV as compared to the experiment by Stamenkovic et al.,²⁷ but roughly similar to that calculated by Rossmeisl et al.³⁶ for the reasons discussed above. Oxygen adsorption does not become important before 1.0 V_{RHE}, where the OH coverage has nearly reached 1/3 ML.

With 25% Ni in the second layer, OH adsorption shifts negatively by \sim 30 mV and moves closer to the experimental curve. The shape of the OH adsorption isotherm for the case of 25% Ni in the second layer agrees well with the voltammetric experiments of Stamenkovic et al.²⁷ This is due to the fact that the variation in OH binding energy on the different sites is not as pronounced as that seen in the case of 50% Ni in the second layer. With 0% Ni in the second layer, OH adsorption moves even closer to the experimental curve. The negative shift of the OH adsorption isotherm agrees qualitatively with the stronger oxygen binding energy on surfaces with low Ni concentration in the second layer, cf., Table 1. It is to be noted that the

surface X-ray scattering (SXS) experiments in the work of Stamenkovic et al.²⁷ show an average composition of 50% Ni in the second layer. In this study, we have chosen the smallest possible unit cell (2×2) to model this, which may not correspond to the real structure. A more detailed analysis of the subsurface Ni structure would be necessary to make a more direct comparison between the results of the model and the experiments.

We note that a langmuir isotherm deviates significantly for OH adsorption from that of the Monte Carlo model, as shown in Figure 6. This is due to the inclusion of geometric effects of site heterogeneity, which causes a split between the stronger binding sites and weaker binding sites. The use of Monte Carlo-based methods merely allows for easy inclusion of these geometric and coadsorption features.

In our model, we have considered only nearest neighbor interactions that have been shown to be reasonably accurate for the system studied here.¹⁰ It is possible that for other more complicated systems, a more systematic study beyond the nearest neighbor might be necessary. In addition, only interactions between OH, O, and H_2O have been included, and interactions with the electrolyte have been ignored. The interactions with the electrolyte are important for adsorbing electrolytes such as H_2SO_4 . We have treated the different reactions within dynamic equilibrium, which corresponds to an infinitely slow scan rate. However, there are features in the voltammogram that are dependent on the scan rate, and these are not easily captured within the present implementation of the model.

CONCLUSIONS

We have simulated the potential-dependent OH and O adsorption on $\text{Pt}(111)$ and Pt_3Ni . The simulations are performed employing DFT calculated interaction and formation energies as input to Monte Carlo simulations. The model predicts that OH adsorbs between 0.65 V_{RHE} and 0.85 V_{RHE}. At 0.9 V_{RHE}, OH starts to get oxidized to O. OH adsorption is accompanied by $\text{H}_2\text{O}(\text{p}1)$ with the $\text{H}_2\text{O}(\text{p}1)$ decorating the edges of the OH– $\text{H}_2\text{O}(\text{p}1)$ islands. As a result, $\text{H}_2\text{O}(\text{p}1)$ has a higher coverage as compared to OH before the formation of the extended $(\sqrt{3} \times \sqrt{3})\text{R}30^\circ$ OH– H_2O . At

higher potentials, further oxidation of OH to O leads to the conversion of H₂O(p1) to its weakly adsorbed H₂O(p2) state. These findings are in good agreement with the ex situ XPS experiments by Wakasaka et al.²⁸

We also simulated OH and O adsorption on Pt₃Ni(111) surfaces terminated by a 1 ML Pt skin and an ordered (2 × 2) subsurface alloy structure with 50%, 25%, or 0% Ni in the second layer. We observed that OH adsorption shifts to more negative potentials as the subsurface Ni concentration is decreased. We also find that the formation of OH in (2 $\sqrt{3}$ × 2 $\sqrt{3}$)R30° OH–H₂O structure is described well by the shift in the formation energy of O.

■ ASSOCIATED CONTENT

S Supporting Information

Details of the calculation method are given. This material is available free of charge via the Internet at <http://pubs.acs.org>.

■ AUTHOR INFORMATION

Corresponding Author

*E-mail: norrskov@stanford.edu.

Notes

The authors declare no competing financial interest.

■ REFERENCES

- (1) Markovic, N.; Gasteiger, H.; Ross, P. N. *J. Electrochem. Soc.* **1997**, *144*, 1591–1597.
- (2) Climent, V.; Gomez, R.; Orts, J. M.; Feliu, J. M. *J. Phys. Chem. B* **2006**, *110*, 11344–11351.
- (3) Bard, A.; Faulkner, L. *Electrochemical Methods: Fundamentals and Applications*; Wiley: New York, 2000.
- (4) Compton, R.; Banks, C. *Understanding Voltammetry*; Imperial College Press: London, 2011.
- (5) Stephens, I. E. L.; Bondarenko, A. S.; Perez-Alonso, F. J.; Calle-Vallejo, F.; Bech, L.; Johansson, T. P.; Jepsen, A. K.; Frydendal, R.; Knudsen, B. P.; Rossmeisl, J.; Chorkendorff, I. *J. Am. Chem. Soc.* **2011**, *133*, 5485–5491.
- (6) Rossmeisl, J.; Nørskov, J. K.; Taylor, C. D.; Janik, M. J.; Neurock, M. *J. Phys. Chem. B* **2006**, *110*, 21833–21839.
- (7) Meng, S. *Surf. Sci.* **2005**, *575*, 300–306.
- (8) Delle Site, L.; Ghiringhelli, L. M.; Andreussi, O.; Donadio, D.; Parrinello, M. *J. Phys.: Condens. Matter* **2007**, *19*, 1–7.
- (9) Otani, M.; Hamada, I.; Sugino, O.; Morikawa, Y.; Okamoto, Y.; Ikeshoji, T. *Phys. Chem. Chem. Phys.* **2008**, *10*, 3609–3612.
- (10) Karlberg, G. S.; Wahnstrom, G. *J. Chem. Phys.* **2005**, *122*, 194705.
- (11) Karlberg, G. S.; Wahnstrom, G.; Clay, C.; Zimbitas, G.; Hodgson, A. *J. Chem. Phys.* **2006**, *124*, 204712.
- (12) Karlberg, G. S.; Wahnstrom, G. *Phys. Rev. Lett.* **2004**, *92*, 136103.
- (13) Thiel, P. A.; Madey, T. E. *Surf. Sci. Rep.* **1987**, *7*, 211–385.
- (14) Michaelides, A.; Hu, P. *J. Chem. Phys.* **2001**, *114*, 513–519.
- (15) Michaelides, A.; Alavi, A.; King, D. A. *J. Am. Chem. Soc.* **2003**, *125*, 2746–2755.
- (16) Anderson, A. B.; Albu, T. V. *Electrochem. Commun.* **1999**, *1*, 203–206.
- (17) Aryanpour, M.; Rai, V.; Pitsch, H. *J. Electrochem. Soc.* **2006**, *153*, E52–E57.
- (18) Rai, V.; Aryanpour, M.; Pitsch, H. *J. Phys. Chem. C* **2008**, *112*, 9760–9768.
- (19) Hammer, B.; Hansen, L.; Nørskov, J. *Phys. Rev. B* **1999**, *59*, 7413–7421.
- (20) Nørskov, J. K.; Rossmeisl, J.; Logadottir, A.; Lindqvist, L.; Kitchin, J. R.; Bligaard, T.; Jonsson, H. *J. Phys. Chem. B* **2004**, *108*, 17886–17892.
- (21) Gillespie, D. T. *J. Comput. Phys.* **1976**, *22*, 403–434.
- (22) Lukkien, J. J.; Segers, J. P. L.; Hilbers, P. A. J.; Gelten, R. J.; Jansen, A. P. *J. Phys. Rev. E* **1998**, *58*, 2598–2610.
- (23) Reese, J. S.; Raimondeau, S.; Vlachos, D. G. *J. Comput. Phys.* **2001**, *173*, 302–321.
- (24) Rai, V.; Pitsch, H.; Novikov, A. *Phys. Rev. E* **2006**, *74*, 046707.
- (25) Viswanathan, V.; Wang, F.; Pitsch, H. *Comput. Sci. Eng.* **2012**, *14* (2), 60–68.
- (26) Wang, J. X.; Markovic, N. M.; Adzic, R. R. *J. Phys. Chem. B* **2004**, *108*, 4127–4133.
- (27) Stamenkovic, V. R.; Fowler, B.; Mun, B. S.; Wang, G. F.; Ross, P. N.; Lucas, C. A.; Markovic, N. M. *Science* **2007**, *315*, 493–497.
- (28) Wakisaka, M.; Suzuki, H.; Mitsui, S.; Uchida, H.; Watanabe, M. *Langmuir* **2009**, *25*, 1897–1900.
- (29) Koper, M. T. M.; Lukkien, J. J. *J. Electroanal. Chem.* **2000**, *485*, 161–165.
- (30) Berna, A.; Climent, V.; Feliu, J. M. *Electrochem. Commun.* **2007**, *9*, 2789–2794.
- (31) Bondarenko, A. S.; Stephens, I. E. L.; Hansen, H. A.; Pérez-Alonso, F. J.; Tripkovic, V.; Johansson, T. P.; Rossmeisl, J.; Nørskov, J. K.; Chorkendorff, I. *Langmuir* **2011**, *27*, 2058–2066.
- (32) Sibert, E.; Faure, R.; Durand, R. *J. Electroanal. Chem.* **2001**, *515*, 71–81.
- (33) Garcia-Araez, N.; Climent, V.; Herrero, E.; Feliu, J. M.; Lipkowski, J. *Electrochim. Acta* **2006**, *51*, 3787–3793.
- (34) Wakisaka, M.; Asizawa, S.; Uchida, H.; Watanabe, M. *Phys. Chem. Chem. Phys.* **2010**, *12*, 4184–4190.
- (35) Björling, A.; Herrero, E.; Feliu, J. M. *J. Phys. Chem. C* **2011**, *115*, 15509–15515.
- (36) Rossmeisl, J.; Karlberg, G. S.; Jaramillo, T.; Nørskov, J. K. *Faraday Discuss.* **2008**, *140*, 337–346.
- (37) Stamenkovic, V.; Mun, B. S.; Mayrhofer, K. J. J.; Ross, P. N.; Markovic, N. M.; Rossmeisl, J.; Greeley, J.; Nørskov, J. K. *Angew. Chem., Int. Ed.* **2006**, *45*, 2897–2901.